ACS Catalysis

pubs.acs.org/acscatalysis

Research Article

Synergistic Effects for Enhanced Catalysis in a Dual Single-Atom Catalyst

Junhong Fu,[¶] Jinhu Dong,[¶] Rui Si,* Keju Sun, Junying Zhang, Mingrun Li, Nana Yu, Bingsen Zhang, Mark G. Humphrey, Qiang Fu,* and Jiahui Huang*

Cite This: *ACS Catal.* 2021, 11, 1952−1961

Read Online

ACCESS | Metrics & More | Article Recommendations | Supporting Information

ABSTRACT: Synergistic effects have been discussed extensively in bimetallic heterogeneous catalysis, but it remains unclear how the effects function at the atomic scale. Here, we report a dual single-atom catalyst (DSAC) Ir_1Mo_1/TiO_2 displaying much greater catalytic chemoselectivity (>96%, at 100% conversion) than comparable single-atom catalysts (SACs) Ir_1/TiO_2 (38%, at 87% conversion) and Mo_1/TiO_2 (no activity) for the hydrogenation of 4-nitrostyrene (4-NS) to 4-vinylaniline (4-VA). Activation of the TiO_2-supported bimetallic carbonyl cluster $Ir_2Mo_2(CO)_{10}(\eta^5\text{-}C_5H_5)_2$ in an Ar atmosphere affords the DSAC Ir_1Mo_1/TiO_2. Characterization of the dual single-atom structure confirms that it consists of well-dispersed Ir single atoms (Ir_1) and Mo single atoms (Mo_1) on TiO_2. Density functional theory studies reveal that Ir_1 sites effect H_2 activation while Mo_1 sites are responsible for 4-NS adsorption, with synergistic cooperation between the two sets of single atoms contributing to the better catalytic performance for the hydrogenation of 4-NS. This work provides a deep understanding of synergistic effects in dual single-atom catalysis.

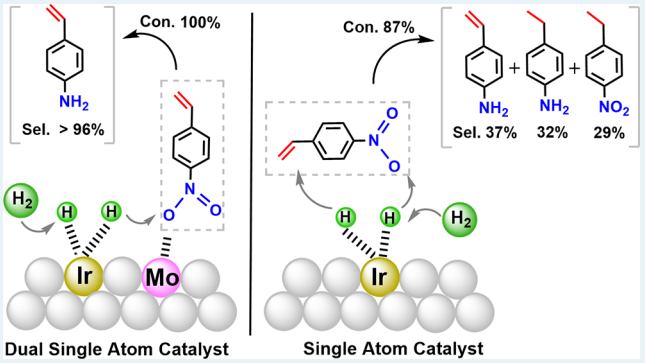

KEYWORDS: *bimetallic catalysis, synergistic effects, single-atom catalyst, dual single-atom catalyst, hydrogenation of nitrostyrene*

INTRODUCTION

Heterogeneous bimetallic catalysis generally involves the cooperation of two metals in a chemical transformation and often displays superior catalytic performance compared to monometallic catalysis due to synergistic effects.[1,2] In particular, supported bimetallic nanoparticles and alloys composed of a noble metal and a non-noble metal have been extensively studied, in which the two types of metals function differently. The noble metals are often the active sites for many reactions, and the non-noble metals influence the noble metal through electronic and geometric interactions, from involvement in the reaction by bonding to the reactants or intermediates, or by creating interfacial sites, which in turn can enhance the catalytic activity and selectivity.[3−6]

Downsizing metal particles to single-metal atoms is a straightforward way to increase metal utilization efficiency, and the resulting single-atom catalysts (SACs) have displayed good catalytic performances in many reactions including CO oxidation,[7,8] the water−gas shift reaction,[9] methane steam reforming,[10] selective nitroarene hydrogenation,[11] and so forth. Instead of one type of single atom (as in SACs), catalysts with a diatomic structure can deliver superior catalytic performance to that of SACs due to cooperation between the two atoms.[12−14] To date, the reported diatomic catalysts mostly feature supported diatomic-pair structures with metal−metal bonds[15−19] or diatomic ensemble structures with M−O−M(M′) linkages.[20−22] The synergistic effect of two sets of single-atom sites (specifically Ni_1 and Ru_1) anchored on CeO_2 in the dry reforming of CH_4 was reported recently; computational studies reveal that Ni_1 activates CH_4 and Ru_1 dissociates CO_2 in the catalytic reaction.[23] However, the synthesis of such dual single-atom catalysts (DSACs) and the understanding of the synergistic effects of the two sets of single-atom sites at the atomic level still remain significant challenges.

Organometallic clusters have long been used as precursors to supported well-defined sub-nanometer clusters.[24−26] The ligands (including carbonyl and organic species) around the organometallic clusters are easily removed in H_2, and the metallic character of the metal clusters is then retained on the support.[27,28] For example, a Pt−Re bimetallic catalyst was prepared through treatment of $Re_2Pt(CO)_{12}$ supported on Al_2O_3 in H_2 and displayed high resistance to deactivation

Received: December 21, 2020
Revised: January 11, 2021
Published: January 29, 2021

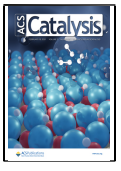

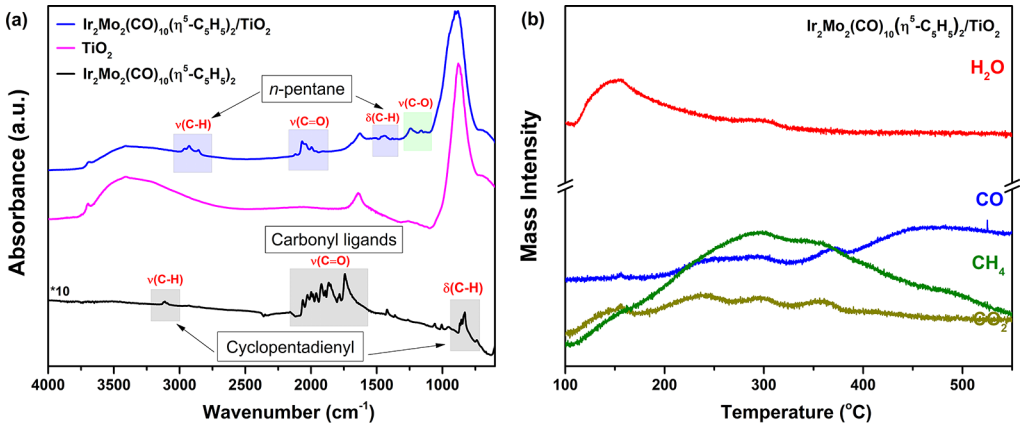

Figure 1. (a) ATR-IR spectra of $Ir_2Mo_2(CO)_{10}(\eta^5\text{-}C_5H_5)_2$, TiO_2, and $Ir_2Mo_2(CO)_{10}(\eta^5\text{-}C_5H_5)_2/TiO_2$. (b) Temperature-programmed desorption results for $Ir_2Mo_2(CO)_{10}(\eta^5\text{-}C_5H_5)_2/TiO_2$ in an Ar flow.

during the catalytic dehydrogenation of methylcyclohexane, due to the role of Re in stabilizing the dispersion of Pt.[29] Shapley and co-workers activated $Ir_2Mo_2(CO)_{10}(\eta^5\text{-}C_5H_5)_2$ on Al_2O_3 in H_2 and the resulting catalyst maintained the intermetallic bonds of the original cluster.[30] In this work, we activate $Ir_2Mo_2(CO)_{10}(\eta^5\text{-}C_5H_5)_2$ on TiO_2 in Ar, affording the DSAC Ir_1Mo_1/TiO_2 that features discrete Ir single atoms (Ir_1) and Mo single atoms (Mo_1) anchored on TiO_2, distinct from the bimetallic structures obtained via H_2 treatment in the previous reports.[27−31] The dual single-atom structure was confirmed by aberration-corrected scanning transmission electron microscopy (STEM), X-ray absorption fine structure (XAFS) spectroscopy, and diffuse reflectance infrared Fourier transform spectroscopy (DRIFTS). Ir_1Mo_1/TiO_2 shows much greater catalytic activity and chemoselectivity in the hydrogenation of 4-nitrostyrene (4-NS) to 4-vinylaniline (4-VA) than the SACs Ir_1/TiO_2 and Mo_1/TiO_2 prepared with the same method from homometallic precursors. Density functional theory (DFT) calculations demonstrate that Ir_1 sites are responsible for H_2 activation and Mo_1 sites are the active sites for the adsorption of 4-NS via the nitro group. The synergistic effects of the two sets of single atoms give rise to an enhanced catalytic performance.

RESULTS AND DISCUSSION

Synthesis and Characterization of the DSAC. Both the DSACs and SACs were synthesized by adsorption and pyrolysis of organometallic precursors (for details, see the Experimental Section). The bimetallic carbonyl cluster $Ir_2Mo_2(CO)_{10}(\eta^5\text{-}C_5H_5)_2$ (Figure S1, synthesized according to the literature[32]) dissolved in dry *n*-pentane was mixed with fresh high-temperature-pretreated TiO_2 (rutile) powder, followed by the removal of the solvent by evacuation, the resultant material being denoted as $Ir_2Mo_2(CO)_{10}(\eta^5\text{-}C_5H_5)_2/TiO_2$. Attenuated total reflectance (ATR) infrared spectroscopy (IR) results (Figure 1a) show that the organometallic precursor is degraded after being deposited on TiO_2, as evidenced by the changes in the ν(C−O) stretching region and the disappearance of bands in the ν(C−H) stretching region that are characteristic of the cyclopentadienyl ligands. The new bands (ranging from 1240 to 1160 cm^{-1}: the green square area in Figure 1a) in the spectral region corresponding to C−O single bonding are tentatively attributed to new organic compounds resulting from the reaction of carbonyl ligands with cyclopentadienyl fragments.[33] The solvent *n*-pentane adsorbed on TiO_2 was not completely removed after evacuation, as shown by the presence of absorption bands corresponding to *n*-pentane (Figures 1a and S2). Further investigations of $Ir_2Mo_2(CO)_{10}(\eta^5\text{-}C_5H_5)_2/TiO_2$ powder heated at 150, 300, and 450 °C in an Ar atmosphere revealed a gradual loss of the carbonyl ligands with increasing temperature, the ligands being completely removed at 450 °C (Figure S3). The sample treated at 450 °C under an Ar atmosphere is denoted as Ir_1Mo_1/TiO_2. Ir_1/TiO_2 and Mo_1/TiO_2 were synthesized by similar methods but instead using $Ir_4(CO)_{12}$ and $Mo(CO)_3(\eta^6\text{-}C_7H_8)$ as the organometallic precursors (Figure S1), respectively. IR spectra of $Ir_4(CO)_{12}$ before and after loading on TiO_2 showed identical absorption bands in the ν(CO) region, meaning that the structure of $Ir_4(CO)_{12}$ is unchanged (Figure S4), while $Mo(CO)_3(\eta^6\text{-}C_7H_8)$ decomposed after loading on TiO_2 as suggested by the disappearance of the ν(CO) absorption bands and a marked reduction in the intensity of the ν(CH) and δ(CH) absorption bands corresponding to $\eta^6\text{-}C_7H_8$ (Figure S5). IR spectra of both Ir_1/TiO_2 and Mo_1/TiO_2 indicated the complete removal of the ligands (Figures S4 and S5).

We also performed temperature-programmed desorption-mass spectrometry (TPD−MS) experiments for $Ir_2Mo_2(CO)_{10}(\eta^5\text{-}C_5H_5)_2/TiO_2$ to ascertain the fate of the organic species during the heating process under Ar (Figure 1b). CO and CO_2 evolution phases are observed at temperatures below 450 °C, which can be assigned to the loss of carbonyl ligands and the reaction of carbonyl ligands with oxygen atoms from the TiO_2 support, respectively. The oxygen loss from TiO_2 gives rise to the generation of oxygen vacancies that are detected by X-ray photoelectron spectroscopy (XPS) and electron paramagnetic resonance (EPR) (Figure S6). The O 1s spectra can be deconvoluted into four peaks, with the peak at 529.3 eV corresponding to the oxygen defects.[34] The EPR signal with a *g* value of 2.003 is attributed to the oxygen vacancy.[34,35] The CH_4 evolution phases can be attributed to the decomposition and loss of $\eta^5\text{-}C_5H_5$. *n*-Pentane adsorbed on the support is also likely to decompose and is believed to also contribute to the evolution of CH_4, CO, and CO_2. TPD−MS studies for TiO_2-supported $Ir_4(CO)_{12}$ and TiO_2-supported $Mo(CO)_3(\eta^6\text{-}C_7H_8)$ are shown in Figure S7. The IR and TPD−MS data confirm the complete removal of the ligands of the precursors following 450 °C treatment in an Ar flow. The metal loadings of Ir (0.14 wt %) and Mo (0.06 wt %) in Ir_1Mo_1/TiO_2 were determined by inductively coupled

https://dx.doi.org/10.1021/acscatal.0c05599
ACS Catal. 2021, 11, 1952−1961

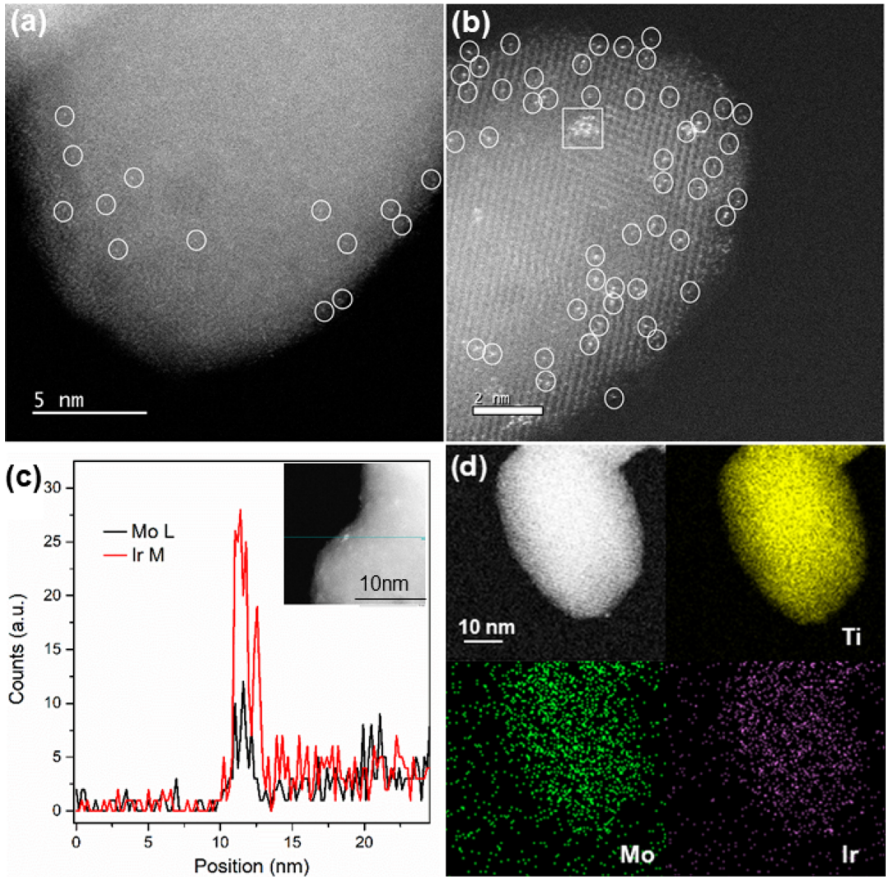

Figure 2. STEM images of (a) Mo_1/TiO_2 and (b) Ir_1Mo_1/TiO_2. The white circles highlight single Ir or Mo atoms, and the white squares contain clusters. (c) LS−EDS of a selected cluster from Ir_1Mo_1/TiO_2 (the inset shows the area at which the line scanning was performed). (d) Elemental mapping of Ir_1Mo_1/TiO_2 by energy-dispersive X-ray spectroscopy.

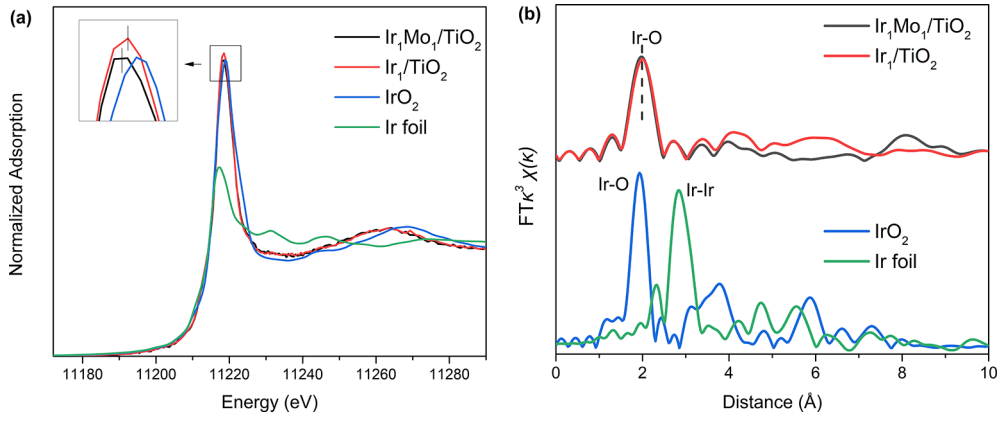

Figure 3. (a) Normalized XANES and (b) Fourier transforms of the EXAFS spectra at the Ir L_3-edge of Ir_1Mo_1/TiO_2, Ir_1/TiO_2, IrO_2, and Ir foil (EXAFS intensity × 1/2).

plasma atomic emission spectroscopy (ICP−AES) analysis (Table S1): the Ir/Mo molar ratio is 1:1, consistent with the atomic ratio of the deposited precursor. The metal loadings in Ir_1/TiO_2 and Mo_1/TiO_2 are close to those of the individual metals in Ir_1Mo_1/TiO_2 (Table S1).

To confirm the local distribution of the Ir and Mo atoms in these structures, aberration-corrected high-angle annular dark-field (AC−HAADF) STEM investigations were performed. Because the atomic numbers of Ti and Mo are relatively close, it is challenging to distinguish Mo single atoms from the TiO_2 surface, particularly when the Mo loading is very low. As shown in the STEM images of Mo_1/TiO_2 (Figures 2a and S8), the Mo_1 is slightly brighter than the lattice Ti atoms, while much brighter and well-dispersed single atoms are clearly observed in the STEM images of Ir_1Mo_1/TiO_2; only a small number of clusters with dimensions of ca. 1 nm were detected (Figures 2b and S9). We note that the AC−HAADF−STEM image does not provide sufficient contrast to distinguish Mo from Ir atoms but it does confirm the atomic dispersion of the Ir and Mo atoms. Linear-scanned energy-dispersive X-ray spectroscopy (LS-EDS) of a selected cluster shows the coexistence of Ir and Mo elements (Figure 2c). The signals

https://dx.doi.org/10.1021/acscatal.0c05599
ACS Catal. 2021, 11, 1952−1961

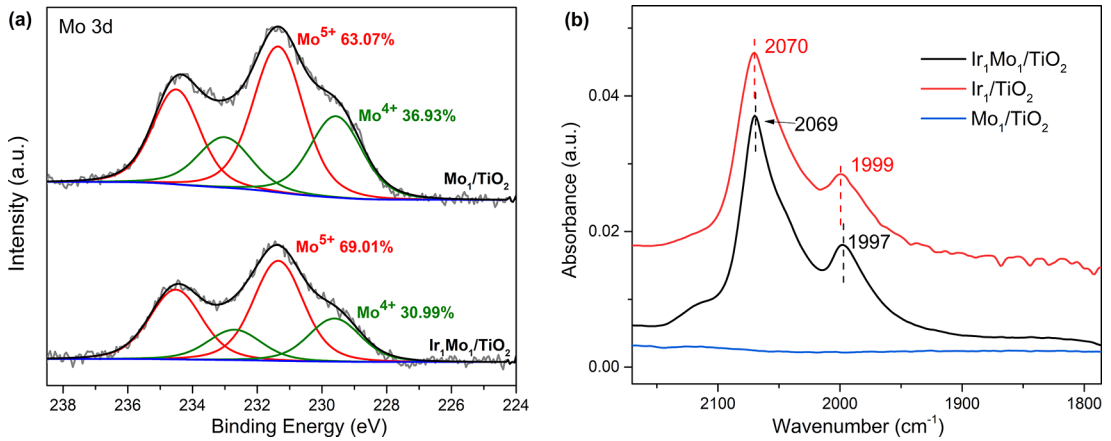

Figure 4. (a) XPS spectra of Mo 3d for Ir_1Mo_1/TiO_2 and Ir_1/TiO_2; (b) DRIFTS spectra of the CO adsorption on Ir_1Mo_1/TiO_2, Ir_1/TiO_2, and Mo_1/TiO_2.

Table 1. Catalytic Data for Hydrogenation of 4-NS[a]

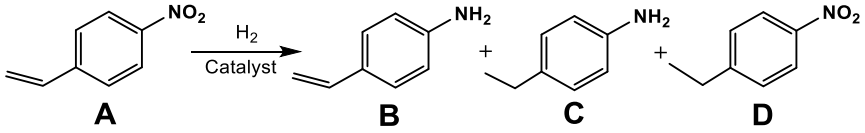

					selectivity[b] (%)		
entry	catalyst	temp. (°C)	time (min)	conv.[b] (%)	B	C	D
1	Ir_1Mo_1/TiO_2	120	60	100	96.3	3.7	0
2	Ir_1Mo_1/TiO_2	120	20	83.2	96.4	2.7	0.8
3	Ir_1/TiO_2	120	60	87.1	37.8	32.8	29.3
4	Mo_1/TiO_2	120	60	0			
5	Ir_1Mo_1/TiO_2	100	240	99.1	97.3	2.7	0
6	Ir_1Mo_1/TiO_2	80	600	90.8	99.2	0.8	0
7	$IrMo/TiO_2$-2[c]	120	60	74.4	50.8	15.8	33.5
8	$IrMo/TiO_2$-3[c]	120	60	18.5	79.8		20.2

[a]Reaction conditions: H_2 pressure (2 MPa), toluene (10 mL), entries 1−4 and 7−8: 0.13 mmol 4-NS, Ir catalyst 0.04 mol %; entries 5−6: 0.19 mmol 4-NS, Ir catalyst 0.04 mol %. [b]Determined by GC−MS. [c]The synthesis procedures are described in the Experimental Section.

are relatively weak due to the small size of the cluster and the low metal loadings. Elemental mapping by energy-dispersive spectroscopy manifested the homogeneous distribution of Mo_1 and Ir_1 over the TiO_2 surface (Figure 2d). STEM images of Ir_1/TiO_2 (Figure S10) reveal that the majority species are Ir_1 atoms, with a small percentage of clusters as in Ir_1Mo_1/TiO_2.

The XAFS technique was used to investigate the electronic and coordination environment of Ir. The normalized X-ray absorption near-edge structure (XANES) profiles at the Ir-L_3 edge of Ir_1Mo_1/TiO_2 and Ir_1/TiO_2 are shown in Figure 3a. Both the absorption energy peaks are very close to that of IrO_2, indicative of structural similarity. The energy of Ir_1Mo_1/TiO_2 is slightly lower than that of Ir_1/TiO_2, indicating a lower oxidation state for Ir in Ir_1Mo_1/TiO_2. The coordination environments of Ir in Ir_1Mo_1/TiO_2 and Ir_1/TiO_2 were determined by extended X-ray absorption fine structure (EXAFS) spectroscopy. Fourier transform (FT) EXAFS spectra at the Ir−L_3 edge show the typical Ir−O coordination environment in the first shell (Figure 3b). The best-fit EXAFS results and parameters are summarized in Figure S11 and Table S2, respectively. The lack of measurable FT peaks corresponding to Ir−Ir, Ir−Mo, and Ir−Ti shells is consistent with an absence of metal−metal bonds in Ir_1Mo_1/TiO_2 and Ir_1/TiO_2 and thereby with the Ir_1 structure that was observed in STEM images. No evidence for Ir−O−Ir and Ir−O−Mo coordination in the second shell was observed, suggesting that the clusters in Ir_1Mo_1/TiO_2 and Ir_1/TiO_2 are composed of loosely isolated Ir atoms, similar to the structure and function of the pseudo-single-atom catalyst 0.08%Pt/FeO_x-R250 reported by Zhang et al.[36]

We note that Shapley and co-workers reported that intermetallic bonds were retained after treatment of $Ir_2Mo_2(CO)_{10}(\eta^5\text{-}C_5H_5)_2$ on Al_2O_3 under a H_2 atmosphere,[30] Gates et al. reported retention of the Ir_4 cluster framework following decarbonylation of $Ir_4(CO)_{12}$ on Al_2O_3 and MgO in H_2,[24,37] and the Ir_4 cluster can be generated from a zeolite-supported Ir complex in H_2.[38,39] We infer that the differing activation procedures (in H_2 or Ar) between these precedents and our studies have resulted in different structures. In the present studies, we propose that after loss of the protecting ligands, the carbonyl cluster $Ir_2Mo_2(CO)_{10}(\eta^5\text{-}C_5H_5)_2$ undergoes decomposition, redistribution, and migration on the TiO_2 surface which is rich in O vacancies (Figure S6) or OH groups (Figure S3) under an Ar atmosphere and then transforms to atomically dispersed Ir and Mo species in a process driven by thermodynamics. Noble metal nanoparticles similarly transforming to single atoms under Ar or O_2 atmospheres have been observed in previous reports.[8,40−46] We therefore propose that treatment of clusters or nanoparticles in a suitable gaseous atmosphere as in the present work could afford single atoms.

https://dx.doi.org/10.1021/acscatal.0c05599
ACS Catal. 2021, 11, 1952−1961

The oxidation states of Mo in Ir_1Mo_1/TiO_2 and Mo_1/TiO_2 were investigated by XPS. The Mo 3d spectra were deconvoluted into Mo^{5+} and Mo^{4+} components for both Ir_1Mo_1/TiO_2 and Mo_1/TiO_2, with the former possessing a slightly higher percentage of Mo^{5+} than the latter (Figure 4a). Due to the low loading of Ir and the overlap of Ir 4f and Ti 3s peaks, it was not possible to obtain effective deconvoluted peaks of Ir $4f_{7/2}$ and $4f_{5/2}$ (Figure S12).

DRIFTS investigations of CO adsorption revealed two bands at 2070/1999 cm^{-1} for Ir_1Mo_1/TiO_2 and at 2069/1997 cm^{-1} for Ir_1/TiO_2 (Figure 4b). The two vibrational bands can be assigned to the symmetric and asymmetric stretching modes of the two carbonyl ligands in the resultant Ir *gem*-dicarbonyl ($Ir(CO)_2$) units. No CO bands were detected for Mo_1/TiO_2. DRIFTS studies of atomically dispersed Ir on a variety of supports have afforded two bands assigned to similar *gem*-dicarbonyl moieties [e.g., MgO (2051/1967 cm^{-1}), γ-Al_2O_3 (2075/1996 cm^{-1}), and $MgAl_2O_4$ (2070/1989 cm^{-1})],[47,48] allowing us to confirm that the Ir atoms in Ir_1Mo_1/TiO_2 and Ir_1/TiO_2 remain atomically dispersed. Additionally, no bands were observed between 1800−1900 cm^{-1}, a region that corresponds to CO adsorbed on large Ir nanoparticles,[20] consistent with the absence of Ir−Ir bonding in both catalysts. Collectively, the AC−HAADF−STEM, XAFS, and DRIFTS studies have confirmed atomically dispersed Ir_1 and/or Mo_1 on Ir_1Mo_1/TiO_2, Ir_1/TiO_2, and Mo_1/TiO_2.

Catalytic Behavior of the DSAC. Selective hydrogenation of 4-NS was used as a probe reaction to evaluate these catalysts. Due to the presence of two reducible groups (nitro and C=C) in a 4-NS molecule, it is challenging to simultaneously achieve high catalytic chemoselectivity and high conversion. In the present work, comparison reactions were carried out at T = 120 °C under a H_2 pressure of 2 MPa, the results being listed in Table 1. When Mo_1/TiO_2 was used as the catalyst, no products were observed. Ir_1Mo_1/TiO_2 displayed an excellent chemoselectivity of 96.3% for 4-VA at 100% conversion of 4-NS and within 1 h. In contrast, under the same reaction conditions, Ir_1/TiO_2 showed poor chemoselectivity (37.8% for 4-VA at 87.1% conversion of 4-NS); two other products, 4-ethylnitrobenzene from selective hydrogenation of the C=C group and 4-ethylaniline from the complete hydrogenation of both nitro and C=C groups, were also formed (29.3 and 32.8% selectivities, respectively). Ir_1Mo_1/TiO_2 retained its excellent chemoselectivity to 4-VA when the hydrogenation reactions were carried out at 80 and 100 °C. No intermediates such as hydroxylamine and azoxy were detected after completion of the reactions.

A comparison with the previous reports on selective hydrogenation of nitrostyrenes shows that the catalytic performance of Ir_1Mo_1/TiO_2 is very competitive (Table S3).[49−53] Recycling stability tests of Ir_1Mo_1/TiO_2 showed a gradual loss of activity (Figure S13). ICP investigations of the used catalyst show that the Ir and Mo metal loadings are greatly reduced (Table S1). It is noteworthy that the excellent selectivity to 4-VA remained even after the ninth run, indicating that the two sets of well-dispersed single atoms remain present. Hydrogenation of various substituted nitroarenes, including those with a range of functional groups (−C=O, −C≡C, −C≡N, $-CH_2OH$, and −X), was also explored to study the broad-spectrum catalytic behavior of the DSAC Ir_1Mo_1/TiO_2. In most cases, the selectivity for the formation of functionalized anilines was excellent (>98% at a nitroarene conversion of ca. 99%: Table S4).

First-Principles Calculations. DFT calculations were carried out to elucidate the dual single-atom structure and understand the superior catalytic behavior of Ir_1Mo_1/TiO_2 toward selective hydrogenation of 4-NS. As shown in Figure S14, model $Ti(M)O_2$ catalysts were constructed by assuming that one or two Ti cations from the rutile TiO_2 (100) surface[54] were substituted by one Ir atom [$Ti(Ir)O_2(100)$] or one Mo atom [$Ti(Mo)O_2(100)$] or one Ir atom and one Mo atom [$Ti(Ir, Mo)O_2(100)$], and the substitution energies of the resultant catalysts were then calculated (Table S4). The results show that two heteroatoms Ir_1 and Mo_1 are more thermodynamically preferable than two Mo atoms or two Ir atoms because the substitution energy of the former (0.55 eV) is lower than those of the latter (0.61 and 1.35 eV). This means that the presence of two distinct single atoms on $TiO_2(100)$ is more favorable than the homometallic single atoms, and this provides additional support for the proposed dual single-atom structure of Ir_1Mo_1/TiO_2. We emphasize here that the role of the small cluster content in Ir_1Mo_1/TiO_2 is ignored in this model because it does not contribute to the enhanced catalytic performance, as we discuss below.

Table 2 lists the adsorption energies of 4-NS via the nitro group, molecular H_2, and dissociated H_2, as well as the reaction barriers for H_2 dissociation on the various model catalysts. Figures S15 and S16 display the adsorption structures of 4-NS and the dissociation process of H_2. The calculation results demonstrate that the adsorption of 4-NS is via the nitro group at the designated surfaces rather than via the vinyl group or the arene ring because of the significantly lower adsorption energies via the nitro group (−0.42 ∼ −1.13 eV) compared to those via the vinyl group or the arene (0 ∼ −0.2 eV). The doped Mo at TiO_2 (100) has a stronger ability than Ir or Ti to adsorb 4-NS via the nitro group, which means that the adsorption of 4-NS via the nitro group would preferentially occur at the Mo atoms. The adsorption of molecular H_2 and dissociated H_2 on Ir is significantly stronger than at Mo or Ti, and the barrier of H_2 dissociation from Ir is much lower than at Mo or Ti, indicating that Ir atoms would activate H_2 rather than Mo or Ti atoms. We therefore propose that during the hydrogenation of 4-NS over Ir_1Mo_1/TiO_2, Mo_1 adsorbs 4-NS via the nitro group and Ir_1 activates H_2.

The more negative adsorption energy of dissociated H_2 (−2.06 eV) compared to that of 4-NS via the nitro group (−0.99 eV) (Table 2) is consistent with a significantly stronger adsorption of H species rather than 4-NS at the Ir atoms. The Ir atoms of $Ti(Ir)O_2(100)$ are indeed likely to be largely or

Table 2. Calculated Adsorption Energies (E_{ads}) of 4-NS via the Nitro Group, Molecular H_2 and Dissociated H_2, and Reaction Barrier for H_2 Dissociation From the Designated Catalyst Site (Unit: eV)

specific site of designated catalyst	E_{ads} 4-NS	E_{ads} molecular H_2	E_{ads} dissociated H_2	barrier for H_2 dissociation
Ti of $TiO_2(100)$	−0.42	−0.04	0.58	1.09
Ir of $Ti(Ir)O_2(100)$	−0.99	−0.90	−2.06	0.46
Mo of $Ti(Mo)O_2(100)$	−1.05	−0.10	0.04	0.85
Ir of $Ti(Ir, Mo)O_2(100)$	–	−0.77	−1.65	0.42
Mo of $Ti(Ir, Mo)O_2(100)$	−1.13	–	–	–

https://dx.doi.org/10.1021/acscatal.0c05599
ACS Catal. 2021, 11, 1952−1961

fully covered by H species, rendering it difficult to adsorb 4-NS via the nitro group. Consequently, both the nitro and the C=C groups of 4-NS can react with the H species on Ir via the Eley−Rideal mechanism, which would likely result in no chemoselectivity between the three possible hydrogenation products. This is consistent with our experimental results, which show that the catalytic hydrogenation of 4-NS over Ir_1/TiO_2 displayed no significant selectivity (4-VA 37.8%, 4-ethylnitrobenzene 29.3%, and 4-ethylaniline 32.8%).

Figure 5 shows the calculated energy profile and reaction pathway for key aspects of the catalytic hydrogenation of 4-NS,

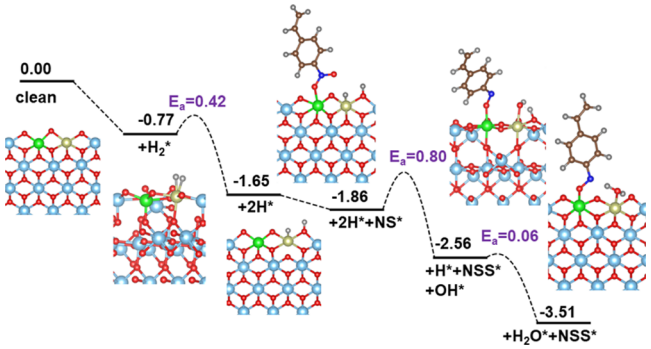

Figure 5. Energy profiles (unit: eV) for catalytic deoxygenation of 4-NS to 4-nitrosostyrene on Ir_1Mo_1/TiO_2. The blue, green, gold, red, gray, deep blue, and brown balls are Ti, Mo, Ir, O, H, N, and C atoms, respectively. NS represents 4-NS and NSS represents 4-nitrosostyrene.

exploiting the well-dispersed Ir_1 and Mo_1 atoms on TiO_2. It is widely accepted that the critical step in hydrogenation of nitrobenzene is deoxygenation of nitrobenzene to nitrosobenzene, which then undergoes multistep reduction to aniline.[55] 4-Nitrosostyrene is hence considered as the final state of this crucial part of the reaction pathway. Adsorption and dissociation of H_2 on Ir_1 decrease the total energy of the system to −1.65 eV. The H_2 molecule then undergoes heterolytic cleavage, resulting in the formation of Ir−H and H−O−Ti bonds. Adsorption of the 4-NS molecule on Mo_1 reduces the total energy further to −1.86 eV. The oxygen atom removed from 4-NS leads to the formation of an Ir−O−H bond, which overcomes a significant energy barrier of 0.80 eV (and is, as a result, the rate-determining step of the reaction; note, though, that the energy barrier here is much lower than that of nitrobenzene to nitrosobenzene on Pd(111) at 1.23 eV).[55] The final step is the formation of water on Ir_1, which is followed by facile desorption. The calculated energy of the reaction is −3.15 eV, indicating that the pathway is thermodynamically feasible. This suggested reaction pathway emphasizes the different roles of Mo_1 and Ir_1 in the catalytic reaction.

Discussion. The combination of experimental and theoretical results presented above has provided a clear picture of the atomic-level synergism operative in the hydrogenation of 4-NS over Ir_1Mo_1/TiO_2. Atomically dispersed Ir_1 and Mo_1 play different roles in the catalytic reaction, Ir_1 activating H_2 and Mo_1 adsorbing 4-NS via the nitro group. The reaction mechanism over Ir_1Mo_1/TiO_2 in the selective hydrogenation of 4-NS is clearly different from the proposed Eley−Rideal mechanism over Ir_1/TiO_2, further confirmed by the wide gap in calculated activation energies (the former: 43.4 ± 6.7 kJ/mol vs the latter: 91.3 ± 6.8 kJ/mol) (Figure S17).

We note that the majority species in the structure of Ir_1Mo_1/TiO_2 are well-dispersed Ir_1 and Mo_1 atoms that are the active sites for the enhanced catalytic performance, but a small percentage of clusters are also observed in the HAADF−STEM images. To rule out the impact of the clusters in the 4-NS hydrogenation reaction, we synthesized $IrMo/TiO_2$-2 via treatment of a mixture of $Ir_4(CO)_{12}$ and $Mo(CO)_3(\eta^6\text{-}C_7H_8)$ on TiO_2 at 450 °C under an Ar atmosphere. The majority species in the structure of $IrMo/TiO_2$-2 are clusters, only a small number of single atoms being present, as is shown in the HAADF-STEM images of $IrMo/TiO_2$-2 (Figure S18). DRIFTS spectra of CO adsorption on $IrMo/TiO_2$-2 (Figure S19) show a pair of bands at 2067/1998 cm^{-1} which can be assigned to atomically dispersed Ir atoms, similar to those in Ir_1Mo_1/TiO_2 and Ir_1/TiO_2. Two bands at 2051 and 2039 cm^{-1} are also observed, corresponding to Ir clusters, according to previous reports.[56] $IrMo/TiO_2$-2 shows a selectivity to 4-VA of 50.8% at a conversion of 74.4% under the same reaction conditions as that of Ir_1Mo_1/TiO_2 (Table 1), which is a significantly poorer performance than that of Ir_1Mo_1/TiO_2. These results strongly suggest that the two sets of highly dispersed single atoms in Ir_1Mo_1/TiO_2 are the active sites for superior catalytic performance, while the large number of clusters in $IrMo/TiO_2$-2 do not favor the desired high selectivity for 4-VA.

We emphasize that because of the limitations of the characterization techniques employed, no unambiguous evidence is available for the existence of bonding (e.g., Ir−O−Mo) between the randomly distributed Ir_1 and Mo_1, but the presence of such interactions can be deduced from the XANES and XPS results: XANES displays a slightly lower oxidation state for Ir in Ir_1Mo_1/TiO_2 than in Ir_1/TiO_2 (Figure 3a), and the XPS Mo 3d spectra show a higher oxidation state for Mo in Ir_1Mo_1/TiO_2 than in Mo_1/TiO_2 (Figure 4a). We conclude that weak interactions exist between the Ir atoms and Mo atoms in Ir_1Mo_1/TiO_2, but the precise nature of their interaction is uncertain and needs further investigation.

In addition, we also activated $Ir_2Mo_2(CO)_{10}(\eta^5\text{-}C_5H_5)_2$ on TiO_2 in hydrogen at 450 °C, the resulting product being denoted as $IrMo/TiO_2$-3. The high-resolution transmission electron microscopy (HRTEM) images of $IrMo/TiO_2$-3 display the presence of nanoclusters (Figure S20), likely resulting from the agglomeration of the original clusters. In the selective hydrogenation of 4-NS, $IrMo/TiO_2$-3 shows a poor selectivity to 4-VA (79.8% at a conversion of 18.5%) under the same reaction conditions as Ir_1Mo_1/TiO_2 (Table 1). We infer that activation of the catalyst in H_2 results in the retention of intermetallic bonds as in Shapley's work,[30] which is not favorable for the targeted high selectivity for hydrogenation of 4-NS.[57]

CONCLUSIONS

We have presented a methodology for the synthesis of DSACs via the activation of supported bimetallic carbonyl clusters in Ar. The well-dispersed dual single-atom structure of Ir_1Mo_1/TiO_2 has been shown to synergistically effect the chemoselective hydrogenation of 4-NS. The highly dispersed discrete single atoms Ir_1 and Mo_1 anchored on a TiO_2 support have been identified by AC−HAADF−STEM, XAFS, and DRIFTS. DSAC Ir_1Mo_1/TiO_2 displays a superior catalytic performance for selective hydrogenation of 4-NS to 4-VA than the single-atom catalyst Ir_1/TiO_2. Computational results suggest that H_2 activation occurs on Ir_1 and 4-NS adsorption via the nitro

https://dx.doi.org/10.1021/acscatal.0c05599
ACS Catal. 2021, 11, 1952−1961

group preferentially occurs on Mo_1, with the synergistic effect of Ir_1 and Mo_1 leading to enhanced catalytic performance. Our work elucidates the atomic-level advantages of DSAC in promoting reaction mechanisms for efficient heterogeneous bimetallic catalysis.

EXPERIMENTAL SECTION

Sample Preparation. Sample synthesis and handling were performed with the exclusion of moisture and air in an argon-filled glovebox. The TiO_2 support (rutile, 25 nm, Aladdin) was treated at 600 °C for 2 h under argon before use. $Ir_2Mo_2(CO)_{10}(\eta^5\text{-}C_5H_5)_2$ (1.7 mg) was dissolved in dry *n*-pentane (50 mL), resulting in the appearance of an orange color. Freshly prepared TiO_2 (1.0 g) was added to the abovementioned solution (the theoretical loading of Ir is about 0.1 wt %), followed by vigorous stirring overnight until the orange color disappeared. The solvent was then removed by evacuation using Schlenk techniques. The resultant solid was heated under argon at 450 °C to afford Ir_1Mo_1/TiO_2. Similarly, TiO_2-supported $Ir_4(CO)_{12}$ (Strem Chemicals) and $Mo(CO)_3(\eta^6\text{-}C_7H_8)$ (Alfa Aesar) were each heated at 450 °C under an argon atmosphere to give Ir_1/TiO_2 and Mo_1/TiO_2; both have a theoretical metal loading of 0.1 wt %. In addition, $IrMo/TiO_2$-2 was synthesized by treatment of a mixture of $Ir_4(CO)_{12}$ and $Mo(CO)_3(\eta^6\text{-}C_7H_8)$ on TiO_2 at 450 °C under an argon atmosphere. $IrMo/TiO_2$-3 was obtained via the activation of $Ir_2Mo_2(CO)_{10}(\eta^5\text{-}C_5H_5)_2$ on TiO_2 at 450 °C under hydrogen. The theoretical metal loadings of Ir and Mo are 0.1 wt % in $IrMo/TiO_2$-2 and $IrMo/TiO_2$-3.

Catalytic Reactions. Hydrogenation of 4-NS was carried out in a stainless-steel autoclave (25 mL) equipped with a pressure gauge and magnetic stirrer (Beijing Shiji Senlang Experimental Instrument Co Ltd). Before the reaction, a mixture of 4-NS (0.13 mmol), toluene (10 mL), and catalyst was placed in a quartz vessel. After being sealed, the autoclave was flushed with hydrogen at least 5 times and then the pressure increased to 2 MPa. The reaction time commenced after reaching the set temperature. After the reaction was complete, the autoclave was cooled to room temperature and the remaining hydrogen gas was discharged. The product was then condensed and analyzed by gas chromatography (7890B) mass spectrometry (5977A) (GCMS, Agilent).

Material Characterization. High-angle annular dark-field (HAADF)−STEM images for Ir_1/TiO_2 and Ir_1Mo_1/TiO_2 were obtained on a JEOL JEM ARM300F instrument with a resolution of 0.063 nm. Samples were dispersed by ultrasonication in ethanol and then dropped on to Cu mesh with carbon microgrids. XPS studies were conducted on a Thermo Fisher ESCALAB 250Xi XPS spectrometer with a monochromatic Al Kα (1486.6 eV) X-ray source. The binding energies of all samples were calibrated by taking the carbon 1s peak as a reference (284.6 eV). The concentrations of iridium and molybdenum were determined by inductively coupled plasma atomic emission spectroscopy (ICP−AES) on a Shimadzu ICPS-8100. Prior to ICP−AES measurement, all samples were dissolved in aqua regia. Attenuated total reflectance infrared spectroscopy (ATR−IR) spectra were collected on a Bruker VERTEX 70 FT-IR spectrometer scaled at 4000 to 640 cm^{-1} with a resolution of 4 cm^{-1}. DRIFTS spectra to assess CO adsorption were recorded on a Bruker VERTEX 70 FT-IR spectrometer. The catalyst was first pretreated at room temperature with N_2 (30 mL min^{-1}) for 0.5 h, followed by a collection of the background spectrum. CO gas was introduced into the reaction cell until the CO adsorption peak intensity no longer increased. N_2 gas was then introduced to the reaction cell to remove CO from the surface of the catalyst, and this was continued until the CO adsorption peak intensity stabilized. At this time, the CO adsorption IR spectra were recorded. TPD−MS was performed on an AutoChem II chemisorption analyzer. Samples were treated in an Ar environment under programmed temperatures: a sample was typically pretreated at 100 °C for 1 h to remove surface H_2O and solvent, and then the temperature was ramped up to 550 °C at a rate of 5 °C/min.

X-ray absorption fine structure (XAFS) spectra at the Ir L_3 (E_0 = 11215 eV) edge were obtained at the BL14W1 beamline of the Shanghai Synchrotron Radiation Facility (SSRF), operating at 3.5 GeV with a "top-up" mode and a constant current of 240 mA. The XAFS data were recorded in the fluorescence mode with a seven-element Ge solid-state detector. The energy was calibrated to the absorption edge of pure Ir powder. Athena and Artemis codes were used to extract the data and fit the profiles. For XANES, the experimental absorption coefficients as a function of energies $\mu(E)$ were processed by background subtraction and normalization procedures and reported as "normalized absorption". For EXAFS, the Fourier-transformed data in R space were analyzed by applying a first-shell approximate model for the Ir−O contribution. The passive electron factor, S_0^2, was determined by fitting the experimental data of the Ir powder and fixing the coordination number (CN) of Ir−Ir for further analysis of the measured samples. The parameters describing the electronic properties (e.g., correction to the photoelectron energy origin, E_0) and local structure environment including CN, bond distance (R), and Debye−Waller factor (σ^2) around the absorbing atoms were allowed to vary during the fit process. The fitted range for k space was selected to be k = 3−10 $Å^{-1}$ (k^3 weighted).

Computational Details. Periodic DFT calculations were performed using the Vienna Ab initio Simulation Package (VASP). The exchange−correlation energy and potential were described by the generalized gradient approximation in the form of PBE. Plane waves with a cutoff of 400 eV were used for projector augmented wave (PAW) potentials. The criteria for the convergence were residual force less than 0.02 eV $Å^{-1}$. The thickness of the vacuum layer was 20 Å. The optimized lattice constants of bulk rutile TiO_2 were a = 4.660 Å and c = 2.974 Å, in good agreement with the experimental values (a = 4.594 Å and c = 2.958 Å). The effect of spin polarization was considered. The k points mesh was set by Monkhorst−Pack methods as 8 × 4 × 1 for the (3 × 1)−Ti(M)O_2 (100) surface with a four-trilayer slab. The upper two trilayers were relaxed, while the lower two trilayers were fixed at their bulk positions.

ASSOCIATED CONTENT

Supporting Information

The Supporting Information is available free of charge at https://pubs.acs.org/doi/10.1021/acscatal.0c05599.

IR spectra, TPD−MS, AC−STEM images, XPS, DFT calculations, ICP, EXAFS fitting results, recycling stability studies, calculated apparent activation energies, and hydrogenation performance of nitroarenes substituted with various groups (PDF)

https://dx.doi.org/10.1021/acscatal.0c05599
ACS Catal. 2021, 11, 1952−1961

AUTHOR INFORMATION

Corresponding Authors

Rui Si − *Shanghai Synchrotron Radiation Facility, Shanghai Institute of Applied Physics, Chinese Academy of Sciences, Shanghai 201204, China;* orcid.org/0000-0003-0732-9688; Email: sirui@mail.sysu.edu.cn

Qiang Fu − *Dalian National Laboratory for Clean Energy, Dalian Institute of Chemical Physics, Chinese Academy of Sciences, Dalian 116023, China; State Key Laboratory of Catalysis, iChEM, Dalian Institute of Chemical Physics, Chinese Academy of Sciences, Dalian 116023, China;* orcid.org/0000-0001-5316-6758; Email: qfu@dicp.ac.cn

Jiahui Huang − *Dalian National Laboratory for Clean Energy, Dalian Institute of Chemical Physics, Chinese Academy of Sciences, Dalian 116023, China;* orcid.org/0000-0002-8522-5430; Email: jiahuihuang@dicp.ac.cn

Authors

Junhong Fu − *Dalian National Laboratory for Clean Energy, Dalian Institute of Chemical Physics, Chinese Academy of Sciences, Dalian 116023, China;* orcid.org/0000-0002-2778-0671

Jinhu Dong − *State Key Laboratory of Catalysis, iChEM, Dalian Institute of Chemical Physics, Chinese Academy of Sciences, Dalian 116023, China*

Keju Sun − *Key Laboratory of Applied Chemistry, College of Environmental and Chemical Engineering, Yanshan University, Qinhuangdao 066004, China;* orcid.org/0000-0001-8791-4646

Junying Zhang − *Dalian National Laboratory for Clean Energy, Dalian Institute of Chemical Physics, Chinese Academy of Sciences, Dalian 116023, China*

Mingrun Li − *State Key Laboratory of Catalysis, iChEM, Dalian Institute of Chemical Physics, Chinese Academy of Sciences, Dalian 116023, China*

Nana Yu − *Dalian National Laboratory for Clean Energy, Dalian Institute of Chemical Physics, Chinese Academy of Sciences, Dalian 116023, China*

Bingsen Zhang − *Shenyang National Laboratory for Materials Science, Institute of Metal Research, Chinese Academy of Sciences, Shenyang 110016, China;* orcid.org/0000-0002-2607-2999

Mark G. Humphrey − *Research School of Chemistry, Australian National University, Canberra, ACT 2601, Australia;* orcid.org/0000-0002-4433-6783

Complete contact information is available at: https://pubs.acs.org/10.1021/acscatal.0c05599

Author Contributions

¶J.F. and J.D. authors contributed equally to this work.

Notes

The authors declare no competing financial interest.

ACKNOWLEDGMENTS

We thank the National Natural Science Foundation of China (grant nos. 21703235 and 21688102), the Strategic Priority Research Program of Chinese Academy of Sciences (grant no. XDB17000000), National Key R&D Program of China (2019YFC1905300), Projects of International Cooperation and Exchanges NSFC (21961142006), and International Postdoctoral Exchange Fellowship Program for the financial support.

REFERENCES

(1) Buchwalter, P.; Rosé, J.; Braunstein, P. Multimetallic Catalysis Based on Heterometallic Complexes and Clusters. *Chem. Rev.* **2015**, *115*, 28−126.

(2) Sankar, M.; Dimitratos, N.; Miedziak, P. J.; Wells, P. P.; Kiely, C. J.; Hutchings, G. J. Designing bimetallic catalysts for a green and sustainable future. *Chem. Soc. Rev.* **2012**, *41*, 8099−8139.

(3) Yu, W.; Porosoff, M. D.; Chen, J. G. Review of Pt-Based Bimetallic Catalysis: From Model Surfaces to Supported Catalysts. *Chem. Rev.* **2012**, *112*, 5780−5817.

(4) Furukawa, S.; Komatsu, T. Intermetallic Compounds: Promising Inorganic Materials for Well-Structured and Electronically Modified Reaction Environments for Efficient Catalysis. *ACS Catal.* **2017**, *7*, 735−765.

(5) Alonso, D. M.; Wettstein, S. G.; Dumesic, J. A. Bimetallic catalysts for upgrading of biomass to fuels and chemicals. *Chem. Soc. Rev.* **2012**, *41*, 8075−8098.

(6) Liu, L.; Lopez-Haro, M.; Lopes, C. W.; Rojas-Buzo, S.; Concepcion, P.; Manzorro, R.; Simonelli, L.; Sattler, A.; Serna, P.; Calvino, J. J.; Corma, A. Structural modulation and direct measurement of subnanometric bimetallic PtSn clusters confined in zeolites. *Nat. Catal.* **2020**, *3*, 628−638.

(7) Qiao, B.; Wang, A.; Yang, X.; Allard, L. F.; Jiang, Z.; Cui, Y.; Liu, J.; Li, J.; Zhang, T. Single-atom catalysis of CO oxidation using Pt_1/FeO_x. *Nat. Chem.* **2011**, *3*, 634−641.

(8) Nie, L.; Mei, D.; Xiong, H.; Peng, B.; Ren, Z.; Hernandez, X. I. P.; DeLaRiva, A.; Wang, M.; Engelhard, M. H.; Kovarik, L.; Datye, A. K.; Wang, Y. Activation of surface lattice oxygen in single-atom Pt/CeO_2 for low-temperature CO oxidation. *Science* **2017**, *358*, 1419−1423.

(9) Yang, M.; Allard, L. F.; Flytzani-Stephanopoulos, M. Atomically Dispersed Au−$(OH)_x$ Species Bound on Titania Catalyze the Low-Temperature Water-Gas Shift Reaction. *J. Am. Chem. Soc.* **2013**, *135*, 3768−3771.

(10) Xie, P.; Pu, T.; Nie, A.; Hwang, S.; Purdy, S. C.; Yu, W.; Su, D.; Miller, J. T.; Wang, C. Nanoceria-Supported Single-Atom Platinum Catalysts for Direct Methane Conversion. *ACS Catal.* **2018**, *8*, 4044−4048.

(11) Lin, L.; Yao, S.; Gao, R.; Liang, X.; Yu, Q.; Deng, Y.; Liu, J.; Peng, M.; Jiang, Z.; Li, S.; Li, Y.-W.; Wen, X.-D.; Zhou, W.; Ma, D. A highly CO-tolerant atomically dispersed Pt catalyst for chemoselective hydrogenation. *Nat. Nanotechnol.* **2019**, *14*, 354−361.

(12) Zhang, J.; Huang, Q.-a.; Wang, J.; Wang, J.; Zhang, J.; Zhao, Y. Supported dual-atom catalysts: Preparation, characterization, and potential applications. *Chin. J. Catal.* **2020**, *41*, 783−798.

(13) Guan, E.; Ciston, J.; Bare, S. R.; Runnebaum, R. C.; Katz, A.; Kulkarni, A.; Kronawitter, C. X.; Gates, B. C. Supported metal pair-site catalysts. *ACS Catal.* **2020**, *10*, 9065−9085.

(14) Pan, Y.; Zhang, C.; Liu, Z.; Chen, C.; Li, Y. Structural Regulation with Atomic-Level Precision: From Single-Atomic Site to Diatomic and Atomic Interface Catalysis. *Matter* **2020**, *2*, 78−110.

(15) Zhu, X.; Zhang, D.; Chen, C.-J.; Zhang, Q.; Liu, R.-S.; Xia, Z.; Dai, L.; Amal, R.; Lu, X. Harnessing the interplay of Fe−Ni atom pairs embedded in nitrogen-doped carbon for bifunctional oxygen electrocatalysis. *Nano Energy* **2020**, *71*, 104597.

(16) Jiao, J.; Lin, R.; Liu, S.; Cheong, W.-C.; Zhang, C.; Chen, Z.; Pan, Y.; Tang, J.; Wu, K.; Hung, S.-F.; Chen, H. M.; Zheng, L.; Lu, Q.; Yang, X.; Xu, B.; Xiao, H.; Li, J.; Wang, D.; Peng, Q.; Chen, C.; Li, Y. Copper atom-pair catalyst anchored on alloy nanowires for selective and efficient electrochemical reduction of CO_2. *Nat. Chem.* **2019**, *11*, 222−228.

(17) Wang, J.; Huang, Z.; Liu, W.; Chang, C.; Tang, H.; Li, Z.; Chen, W.; Jia, C.; Yao, T.; Wei, S.; Wu, Y.; Li, Y. Design of N-Coordinated Dual-Metal Sites: A Stable and Active Pt-Free Catalyst for Acidic Oxygen Reduction Reaction. *J. Am. Chem. Soc.* **2017**, *139*, 17281−17284.

(18) Lu, Z.; Wang, B.; Hu, Y.; Liu, W.; Zhao, Y.; Yang, R.; Li, Z.; Luo, J.; Chi, B.; Jiang, Z.; Li, M.; Mu, S.; Liao, S.; Zhang, J.; Sun, X.

An Isolated Zinc−Cobalt Atomic Pair for Highly Active and Durable Oxygen Reduction. *Angew. Chem., Int. Ed.* **2019**, *58*, 2622−2626.
(19) Zhang, M.; Hu, Z.; Gu, L.; Zhang, Q.; Zhang, L.; Song, Q.; Zhou, W.; Hu, S. Electrochemical conversion of CO_2 to syngas with a wide range of CO/H_2 ratio over Ni/Fe binary single-atom catalysts. *Nano Res.* **2020**, *13*, 3206−3211.
(20) Zhao, Y.; Yang, K. R.; Wang, Z.; Yan, X.; Cao, S.; Ye, Y.; Dong, Q.; Zhang, X.; Thorne, J. E.; Jin, L.; Materna, K. L.; Trimpalis, A.; Bai, H.; Fakra, S. C.; Zhong, X.; Wang, P.; Pan, X.; Guo, J.; Flytzani-Stephanopoulos, M.; Brudvig, G. W.; Batista, V. S.; Wang, D. Stable iridium dinuclear heterogeneous catalysts supported on metal-oxide substrate for solar water oxidation. *Proc. Natl. Acad. Sci. U. S. A.* **2018**, *115*, 2902−2907.
(21) Yang, Y.; Qian, Y.; Li, H.; Zhang, Z.; Mu, Y.; Do, D.; Zhou, B.; Dong, J.; Yan, W.; Qin, Y.; Fang, L.; Feng, R.; Zhou, J.; Zhang, P.; Dong, J.; Yu, G.; Liu, Y.; Zhang, X.; Fan, X. O-coordinated W-Mo dual-atom catalyst for pH-universal electrocatalytic hydrogen evolution. *Sci. Adv.* **2020**, *6*, No. eaba6586.
(22) Wang, H.; Liu, J.-X.; Allard, L. F.; Lee, S.; Liu, J.; Li, H.; Wang, J.; Wang, J.; Oh, S. H.; Li, W.; Flytzani-Stephanopoulos, M.; Shen, M.; Goldsmith, B. R.; Yang, M. Surpassing the single-atom catalytic activity limit through paired Pt-O-Pt ensemble built from isolated Pt_1 atoms. *Nat. Commun.* **2019**, *10*, 3808.
(23) Tang, Y.; Wei, Y.; Wang, Z.; Zhang, S.; Li, Y.; Nguyen, L.; Li, Y.; Zhou, Y.; Shen, W.; Tao, F. F.; Hu, P. Synergy of Single-Atom Ni_1 and Ru_1 Sites on CeO_2 for Dry Reforming of CH_4. *J. Am. Chem. Soc.* **2019**, *141*, 7283−7293.
(24) Xu, Z.; Xiao, F.-S.; Purnell, S. K.; Alexeev, O.; Kawi, S.; Deutsch, S. E.; Gates, B. C. Size-dependent catalytic activity of supported metal clusters. *Nature* **1994**, *372*, 346−348.
(25) Kulkarni, A.; Lobo-Lapidus, R. J.; Gates, B. C. Metal clusters on supports: synthesis, structure, reactivity, and catalytic properties. *Chem. Commun.* **2010**, *46*, 5997−6015.
(26) Gates, B. C. Supported Metal Clusters: Synthesis, Structure, and Catalysis. *Chem. Rev.* **1995**, *95*, 511−522.
(27) Alexeev, O. S.; Gates, B. C. Supported Bimetallic Cluster Catalysts. *Ind. Eng. Chem. Res.* **2003**, *42*, 1571−1587.
(28) Guzman, J.; Gates, B. C. Supported molecular catalysts: metal complexes and clusters on oxides and zeolites. *Dalton Trans.* **2003**, 3303−3318.
(29) Fung, A. S.; Kelley, M. J.; Koningsberger, D. C.; Gates, B. C. γ-Al_2O_3-Supported Re−Pt Cluster Catalyst Prepared from $[Re_2Pt(CO)_{12}]$: Characterization by Extended X-ray Absorption Fine Structure Spectroscopy and Catalysis of Methylcyclohexane Dehydrogenation. *J. Am. Chem. Soc.* **1997**, *119*, 5877−5887.
(30) Shapley, J. R.; Uchiyama, W. S.; Scott, R. A. Bimetallic catalysts from alumina-supported molybdenum-iridium clusters. *J. Phys. Chem.* **1990**, *94*, 1190−1196.
(31) Shapley, J. R.; Hardwick, S. J.; Foose, D. S.; Stucky, G. D.; Churchill, M. R.; Bueno, C.; Hutchinson, J. P. Bimetallic catalysts from pseudotetrahedral iridium-tungsten clusters. Synthesis and crystal structures of $(\eta^5\text{-}C_5H_5)WIr_3(CO)_{11}$ and $(\eta^5\text{-}C_5H_5)_2W_2Ir_2(CO)_{10}$. *J. Am. Chem. Soc.* **1981**, *103*, 7383−7385.
(32) Lucas, N. T.; Humphrey, M. G.; Hockless, D. C. R. Mixed-metal cluster chemistry V. Syntheses and X-ray crystal structure of $Cp_2Mo_2Ir_2(\mu_3\text{-}CO)(\mu\text{-}CO)_5(CO)_4$. *J. Organomet. Chem.* **1997**, *535*, 175−181.
(33) Flores-Escamilla, G. A.; Fierro-Gonzalez, J. C. Infrared spectroscopic study of dimethyl ether carbonylation catalysed by TiO_2-supported rhodium carbonyls. *Catal. Sci. Technol.* **2015**, *5*, 843−850.
(34) Liu, N.; Xu, M.; Yang, Y.; Zhang, S.; Zhang, J.; Wang, W.; Zheng, L.; Hong, S.; Wei, M. $Au^{\delta-}-O_v-Ti^{3+}$ Interfacial Site: Catalytic Active Center toward Low-Temperature Water Gas Shift Reaction. *ACS Catal.* **2019**, *9*, 2707−2717.
(35) Tian, S.; Gong, W.; Chen, W.; Lin, N.; Zhu, Y.; Feng, Q.; Xu, Q.; Fu, Q.; Chen, C.; Luo, J.; Yan, W.; Zhao, H.; Wang, D.; Li, Y. Regulating the Catalytic Performance of Single-Atomic-Site Ir Catalyst for Biomass Conversion by Metal−Support Interactions. *ACS Catal.* **2019**, *9*, 5223−5230.
(36) Wei, H.; Liu, X.; Wang, A.; Zhang, L.; Qiao, B.; Yang, X.; Huang, Y.; Miao, S.; Liu, J.; Zhang, T. FeO_x-supported platinum single-atom and pseudo-single-atom catalysts for chemoselective hydrogenation of functionalized nitroarenes. *Nat. Commun.* **2014**, *5*, 5634.
(37) Alexeev, O.; Panjabi, G.; Gates, B. C. Partially Decarbonylated Tetrairidium Clusters on γ-Al_2O_3: Structural Characterization and Catalysis of Toluene Hydrogenation. *J. Catal.* **1998**, *173*, 196−209.
(38) Lu, J.; Aydin, C.; Browning, N. D.; Gates, B. C. Hydrogen Activation and Metal Hydride Formation Trigger Cluster Formation from Supported Iridium Complexes. *J. Am. Chem. Soc.* **2012**, *134*, 5022−5025.
(39) Lu, J.; Serna, P.; Aydin, C.; Browning, N. D.; Gates, B. C. Supported Molecular Iridium Catalysts: Resolving Effects of Metal Nuclearity and Supports as Ligands. *J. Am. Chem. Soc.* **2011**, *133*, 16186−16195.
(40) Wei, S.; Li, A.; Liu, J.-C.; Li, Z.; Chen, W.; Gong, Y.; Zhang, Q.; Cheong, W.-C.; Wang, Y.; Zheng, L.; Xiao, H.; Chen, C.; Wang, D.; Peng, Q.; Gu, L.; Han, X.; Li, J.; Li, Y. Direct observation of noble metal nanoparticles transforming to thermally stable single atoms. *Nat. Nanotechnol.* **2018**, *13*, 856−861.
(41) Jones, J.; Xiong, H.; DeLaRiva, A. T.; Peterson, E. J.; Pham, H.; Challa, S. R.; Qi, G.; Oh, S.; Wiebenga, M. H.; Pereira Hernández, X. I.; Wang, Y.; Datye, A. K. Thermally stable single-atom platinum-on-ceria catalysts via atom trapping. *Science* **2016**, *353*, 150−154.
(42) Moliner, M.; Gabay, J. E.; Kliewer, C. E.; Carr, R. T.; Guzman, J.; Casty, G. L.; Serna, P.; Corma, A. Reversible Transformation of Pt Nanoparticles into Single Atoms inside High-Silica Chabazite Zeolite. *J. Am. Chem. Soc.* **2016**, *138*, 15743−15750.
(43) Lang, R.; Xi, W.; Liu, J.-C.; Cui, Y.-T.; Li, T.; Lee, A. F.; Chen, F.; Chen, Y.; Li, L.; Li, L.; Lin, J.; Miao, S.; Liu, X.; Wang, A.-Q.; Wang, X.; Luo, J.; Qiao, B.; Li, J.; Zhang, T. Non defect-stabilized thermally stable single-atom catalyst. *Nat. Commun.* **2019**, *10*, 234.
(44) Jeong, H.; Bae, J.; Han, J. W.; Lee, H. Promoting Effects of Hydrothermal Treatment on the Activity and Durability of Pd/CeO_2 Catalysts for CO Oxidation. *ACS Catal.* **2017**, *7*, 7097−7105.
(45) Aitbekova, A.; Wu, L.; Wrasman, C. J.; Boubnov, A.; Hoffman, A. S.; Goodman, E. D.; Bare, S. R.; Cargnello, M. Low-Temperature Restructuring of CeO_2-Supported Ru Nanoparticles Determines Selectivity in CO_2 Catalytic Reduction. *J. Am. Chem. Soc.* **2018**, *140*, 13736−13745.
(46) Jeong, H.; Lee, G.; Kim, B.-S.; Bae, J.; Han, J. W.; Lee, H. Fully Dispersed Rh Ensemble Catalyst To Enhance Low-Temperature Activity. *J. Am. Chem. Soc.* **2018**, *140*, 9558−9565.
(47) Lu, J.; Aydin, C.; Browning, N. D.; Gates, B. C. Oxide- and Zeolite-Supported Isostructural $Ir(C_2H_4)_2$ Complexes: Molecular-Level Observations of Electronic Effects of Supports as Ligands. *Langmuir* **2012**, *28*, 12806−12815.
(48) Lu, Y.; Wang, J.; Yu, L.; Kovarik, L.; Zhang, X.; Hoffman, A. S.; Gallo, A.; Bare, S. R.; Sokaras, D.; Kroll, T.; Dagle, V.; Xin, H.; Karim, A. M. Identification of the active complex for CO oxidation over single-atom Ir-on-$MgAl_2O_4$ catalysts. *Nat. Catal.* **2019**, *2*, 149−156.
(49) Song, J.; Huang, Z.-F.; Pan, L.; Li, K.; Zhang, X.; Wang, L.; Zou, J.-J. Review on selective hydrogenation of nitroarene by catalytic, photocatalytic and electrocatalytic reactions. *Appl. Catal., B* **2018**, *227*, 386−408.
(50) Mao, J.; Chen, W.; Sun, W.; Chen, Z.; Pei, J.; He, D.; Lv, C.; Wang, D.; Li, Y. Rational Control of the Selectivity of a Ruthenium Catalyst for Hydrogenation of 4-Nitrostyrene by Strain Regulation. *Angew. Chem., Int. Ed.* **2017**, *56*, 11971−11975.
(51) Wang, L.; Guan, E.; Zhang, J.; Yang, J.; Zhu, Y.; Han, Y.; Yang, M.; Cen, C.; Fu, G.; Gates, B. C.; Xiao, F.-S. Single-site catalyst promoters accelerate metal-catalyzed nitroarene hydrogenation. *Nat. Commun.* **2018**, *9*, 1362.
(52) Tan, Y.; Liu, X. Y.; Zhang, L.; Wang, A.; Li, L.; Pan, X.; Miao, S.; Haruta, M.; Wei, H.; Wang, H.; Wang, F.; Wang, X.; Zhang, T. ZnAl-Hydrotalcite-Supported Au_{25} Nanoclusters as Precatalysts for

https://dx.doi.org/10.1021/acscatal.0c05599
ACS Catal. 2021, 11, 1952−1961

Chemoselective Hydrogenation of 3-Nitrostyrene. *Angew. Chem., Int. Ed.* **2017**, *56*, 2709−2713.
(53) Corma, A.; Serna, P. Chemoselective Hydrogenation of Nitro Compounds with Supported Gold Catalysts. *Science* **2006**, *313*, 332−334.
(54) Perron, H.; Domain, C.; Roques, J.; Drot, R.; Simoni, E.; Catalette, H. Optimisation of accurate rutile TiO_2 (110), (100), (101) and (001) surface models from periodic DFT calculations. *Theor. Chem. Acc.* **2007**, *117*, 565−574.
(55) Zhang, L.; Shao, Z.-J.; Cao, X.-M.; Hu, P. Insights into Different Products of Nitrosobenzene and Nitrobenzene Hydrogenation on Pd(111) under Realistic Reaction Conditions. *J. Phys. Chem. C* **2018**, *122*, 20337−20350.
(56) Chen, P.; Lu, J.-Q.; Xie, G.-Q.; Hu, G.-S.; Zhu, L.; Luo, L.-F.; Huang, W.-X.; Luo, M.-F. Effect of reduction temperature on selective hydrogenation of crotonaldehyde over Ir/TiO_2 catalysts. *Appl. Catal., A* **2012**, *433*−*434*, 236−242.
(57) Zhang, S.; Chang, C.-R.; Huang, Z.-Q.; Li, J.; Wu, Z.; Ma, Y.; Zhang, Z.; Wang, Y.; Qu, Y. High Catalytic Activity and Chemoselectivity of Sub-nanometric Pd Clusters on Porous Nanorods of CeO_2 for Hydrogenation of Nitroarenes. *J. Am. Chem. Soc.* **2016**, *138*, 2629−2637.

https://dx.doi.org/10.1021/acscatal.0c05599
ACS Catal. 2021, 11, 1952−1961